Photo-degradation in bulk heterojunction organic solar cells using a fullerene or a non-fullerene derivative electron acceptor

Amina Labiod, Olzhas A Ibraikulov, Sylvie Dabos-Seignon, Stéphanie Ferry, Benoît Heinrich, Stéphane Méry, Sadiara Fall, Thomas Heiser, Clément Cabanetos, Nicolas Leclerc, et al.

▶ To cite this version:

Amina Labiod, Olzhas A Ibraikulov, Sylvie Dabos-Seignon, Stéphanie Ferry, Benoît Heinrich, et al.. Photo-degradation in bulk heterojunction organic solar cells using a fullerene or a non-fullerene derivative electron acceptor. Organic Electronics, 2022, 107, pp.106549. ⟨10.1016/j.orgel.2022.106549⟩. ⟨hal-03795533⟩

HAL Id: hal-03795533
https://hal.science/hal-03795533v1

Submitted on 4 Oct 2022

Photo-degradation in bulk heterojunction organic solar cells using a fullerene or a non-fullerene derivative electron acceptor.

Amina Labiod[1], Olzhas. A. Ibraikulov[1], Sylvie Dabos- Seignon[2], Stéphanie Ferry[3], Benoît Heinrich[4], Stéphane Méry[4], Sadiara Fall[1], Thomas Heiser[1], Clément Cabanetos[2], Nicolas Leclerc[3], et Patrick Lévêque[1*].

[1]Laboratoire des sciences de l'ingénieur, de l'informatique et de l'imagerie (ICube), Université de Strasbourg, CNRS, 23 rue du Loess, Strasbourg, 67037, France.
[2]Université d'Angers, CNRS, MOLTECH-ANJOU, SFR MATRIX, 49000, Angers, France
[3]Institut de Chimie et Procédés pour l'Energie, l'Environnement et la Santé (ICPEES), Université de Strasbourg, CNRS, 25 rue Becquerel, 67087 Strasbourg, Cedex 02, France.
[4]Institut de Physique et de Chimie des Matériaux de Strasbourg (IPCMS), Université de Strasbourg, CNRS, 23 rue du Loess, 67034 Strasbourg, Cedex 2, France.

*patrick.leveque@unistra.fr

Abstract :

The use of Non-Fullerene Acceptors (NFAs) in the active layer of organic solar cells (OSCs) has made it possible to exceed 18% conversion efficiency. However, OSCs still present stability issues under operational conditions that need to be surpassed for their industrialization. In this work, we investigated binary and ternary blends to examine their efficiency and their stability as active layers of OSCs. We used a fluorinated polymer (PF2) as an electron donor and two different electron acceptors, a fullerene derivative ($PC_{71}BM$) and a NFA (EH-IDTBR). We demonstrated that using EH-IDTBR instead of $PC_{71}BM$ leads to a decrease in efficiency attributed to the low out-of-plane electron mobility measured in the blend. However, using EH-IDTBR as single electron-acceptor significantly enhanced the OSCs stability under continuous illumination. Ternary blends were tested to reach simultaneously a high efficiency and a long-term stability. The best efficiency/stability compromise appeared to be when using EH-IDTBR only as electron-acceptor. We identified changes in the main charge-carrier recombination mechanism in photo-degraded devices from bimolecular in low EH-IDTBR content blends to trap-assisted in high EH-IDTBR ones. Finally, the blend morphology at a nanometer scale appeared as stable in high EH-IDTBR content blends while photo-degradation impacted significantly the morphology of the low EH-IDTBR content blend.

Keywords:

Organic photovoltaics; photo-degradation; ternary blend

1. Introduction:

Organic solar cells (OSCs) have received a lot of attention in the photovoltaic field due to their interesting properties compared to their inorganic counterparts such as flexibility, lightweight, semi-transparency, low cost and large-scale manufacturing in roll-to-roll processes. Starting from the bulk heterojunction (BHJ) concept discovery [1], the Power Conversion Efficiency (PCE) of OSCs has increased from roughly 1% up to more than 18% nowadays [2]. In the BHJ configuration, the electron donor (D) and the electron acceptor (A) materials are intimately intermixed, forming nano-scaled continuous interpenetrating networks. This BHJ configuration enhances the free charge carriers' generation and transport. Fullerene derivatives have been widely used as electron acceptors in OSCs [3–5], thanks to their large electron affinity and high electron mobility with an isotropic charge transport. However, fullerene derivatives suffer from a weak absorption in the visible spectrum and from energy levels that are difficult to adjust. A strong bottleneck to reach PCEs higher than 10% with OSCs has long been the availability of alternative electron acceptors.

Researchers have made great efforts to design novel π-conjugated small molecules with adjusted frontier energy levels, high electron mobility and broad light absorption range. In the last two years, progress was made in non-fullerene acceptors (NFAs) design in order to overcome the 10% PCE barrier. Yuan et al. introduced DAD fused core in the push-pull structure of Y5 (BTP) [6]. Its fluorinated version (BTP-4F), also known as Y6, has emerged as a promising NFA giving a certified PCE approaching 15% in binary blends [7]. In order to promote the BHJ supramolecular organization to enhance the exciton dissociation and charge carriers transport and reduce the nonradiative energy losses, researchers adopted the ternary strategy by adding a third component to the main D/A binary blend [8,9]. The third component can be either a donor [10,11] or an acceptor [12–14], a polymer, a small molecule, or even a nanoparticle [15]. Recently, Yanming et al. have made chemical structure adjustments on Y6 by modifying the branched alkyl chain [16], leading to a high efficiency in single junctions, around 18.60% (certified at 18.20%) in both binary [2] and ternary [17] blends. With the increasing interest in the ternary blends very recently, the F-BTA3 NFA has been added as the third component to the PBQx-TF:eC9-2Cl binary blend, which improved the photovoltaic performances and led to the record PCE of 19% in single-junction OSCs [18]. Moreover, tandem OSCs using NFAs have reached PCEs exceeding 18% [19,20].

A high PCE is not the only important property when considering a photovoltaic system. PV systems must operate effectively for long periods and in different environmental conditions. The Levelized Cost Of Energy (LCOE) [21,22] is defined as the total lifetime cost divided by the energy produced by the PV system. The LCOE is then strongly affected by the operating stability, which represents today a major challenge for OSCs. During their entire life, PV systems do not operate with the same efficiency. Jordan et al. [23] called the “degradation process” the progressive deterioration of the appearance, the photovoltaic performances and the safety of PV systems. It induces a decrease in efficiency over the years, owing to stress sources as thermal cycling, humidity, irradiation and mechanical shocks. Therefore, the investigation of PV system degradation has gained more interest, encouraging researchers of the National Renewable Energy Laboratory (NREL) [24] to analyze more than 11000 degradation rates. They found a median degradation rate of 0.5–0.6%/year and a mean of 0.8–0.9%/year for crystalline silicon high-quality technologies. However, this rate could get higher in a hot and humid environment. The classical PV systems lifetime (T_{80}) warrantied by the manufacturers is about 20-25 years. That means in 25 years the efficiency decreases down to 80% of its initial value.

The standard qualification tests (ex: IEC 61215-crystalline silicon), developed initially by the Jet Propulsion Laboratory (JPL) in the early 1980s [25] are used under stress sources for a long duration to predict the PV system lifetime. However, the data obtained using these tests are not sufficient to deduce the PV system lifetime. Nevertheless, an accelerated test could predict the lifetime by artificially speeding up stress factors until the PV system failure. For instance, the empirical temperature-humidity acceleration model of Desombre [26] was used later in the JPL corrosion model [27]. The accelerated high temperature could damage the materials of the PV system. Further, the UV irradiation containing high energy photons could lead to degradation which does not realistically represent the solar irradiation.

Although the organic semiconductors are more sensitive to environmental conditions than their inorganic counterparts, there is no well-defined standard test for OSC lifetime. During the first three international summits on organic photovoltaic stability (ISOS), test protocols under stress have been established to increase the amount of stability data [28]. The OSC lifetime was investigated, for most cases, under continuous standard illumination of 100 mW/cm² and long operational lifetimes (T_{80}) have been demonstrated from hundreds of hours [29] to thousands of hours [30]. Du et al. found a predicted lifetime approaching ten years [31]. Very recently, a predicted lifetime as high as 30 years has even been published for a Non-Fullerene Acceptor (NFA) based OSC [32]. The OSC degradation phenomena, and the factors causing it, were highlighted in the dark and continuous simulated AM 1.5 irradiation, under either air exposure or controlled environment. Degradation can be due to the device structure. For instance, Kawano et al. concluded that the degradation of the OSC is related to the water diffusion into PEDOT:PSS layer resulting in the series resistance increase [33]. The OSC performance deterioration could also be related to chemical modification of the active layer. The $PC_{61}BM$-based OSC exposed to a sun-equivalent white light source for 120 hours and under inert conditions showed the induced fullerene dimerization [34]. The exposure of $PC_{61}BM$-based OSC to natural outdoor conditions in the Negev-desert also induced the fullerene dimerization [35]. Accelerated tests have also been used for studying the OSC stability/degradation. Exposing OSCs to high light-intensity, so-called «photo-degradation » could accelerate their degradation process until the failure and enable an estimation of the lifetime [36].

In this work, we used a low bandgap fluorinated copolymer (PF2) [37] as an electron donor and ([6,6]-phenyl-C71-butyric acid methyl ester) ($PC_{71}BM$) as an electron acceptor. PF2 is known to self-organize in crystalline lamellas with face-on preferential orientation. That results in high hole mobility and the formation of pure domains in [PF2:$PC_{71}BM$] BHJ, leading to the efficient transport of charge carriers with limited trap-assisted recombination. In addition, PF2 showed good light-absorption complementarity with $PC_{71}BM$. On the one hand, due to the promising characteristics of the [PF2:$PC_{71}BM$] blend, an efficiency of above 10% has already been reported by our team [38]. On the other hand, encapsulated devices showed a relatively low stability with devices stored in the dark losing almost 40% of their initial PCE in 200 hours. In the present work, we also used EH-IDTBR [39] as an alternative electron-acceptor with PF2. EH-IDTBR is one of the most reported small-molecule NFA, owing to its high electron affinity contributing to the high open-circuit voltage (V_{oc}) [40]. Moreover, EH-IDTBR has improved the domain crystallinity in ternary blends [PTB7-TH:F8IC:EH-IDTBR] reducing the energetic disorder and leading to a high PCE of 12.3% [41]. The stability of blends using EH-IDTBR as electron-acceptor is its most interesting property. It was shown that OSCs based on EH-IDTBR in blend with a low-bandgap donor polymer (PffBT4T-2DT) under continuous white light illumination had more than 90% of their initial PCE after 4000h [42]. Preliminary stability tests were also conducted on [PF2:EH-IDTBR] devices under continuous AM 1.5 illumination. These devices had a lower PCE around 6%. Encapsulated [PF2:EH-IDTBR] devices showed a relative loss in efficiency lower than 10% after 300 h continuous illumination [43]. In the present work, we decided to explore the properties of PF2/PCBM/EH-IDTBR ternary blends with the goal to identify the best compromise in terms of the high PCE obtained on [PF2:$PC_{71}BM$] devices and the promising stability observed on [PF2:EH-IDTBR] devices. The stability was estimated using accelerated photo-degradation on non-encapsulated devices in an inert atmosphere. Several binary ([PF2:$PC_{71}BM$] and [PF2:EH-IDTBR]) and ternary [PF2:$PC_{71}BM$:EH-IDTBR] blends were tested. The photovoltaic performances as a function of degradation time were measured. Fresh and aged samples were studied as a function of light-intensity to highlight the main charge-carrier recombination mechanism in each case. Finally, the fresh and aged samples' morphology were investigated by atomic force microscopy (AFM) to correlate the morphology evolution with the performance degradation.

2. Experimental details:

2.1. UV-visible absorption spectra.

UV-Vis absorption spectra were measured in the solid-state in the 350-800 nm wavelength range. Indium tin oxide (ITO) glass substrates (purchased from Luminescence Technology (LumTech)) were pre-cleaned in an ultrasonic bath with sequentially hellmanex, deionized water, acetone and isopropanol at 45°C for 15 minutes. Then, substrates were dried with nitrogen and treated in an ultraviolet-ozone chamber (Novascan Digital UV Ozone System_PSD Series) for 30 min. ZnO nanoparticles (2.5 wt% in 2-propanol) from Avantama were filtered through a 0.45 µm polyvinylidene difluoride (PVDF) membrane filter and spin-coated at 5000 rpm for 60 s onto the pre-cleaned glass:ITO substrates. Subsequently, the ZnO thin film was annealed at 110°C for 10 min in air, and the thickness was about 20 nm. The electron-donor polymer PF2 (M_n = 47 kg/mol, M_W = 164 kg/mol and Đ = 3.4) was synthesized and characterized according to the already published procedure [37]. The electron-acceptors, $PC_{71}BM$ (from SOLENNE B.V, 99%) and the small molecule EH-IDTBR (from 1-Material) were used as received. A PF2 and EH-IDTBR solutions in *o*-DCB with a concentration of 4.5 mg/ml and 10 mg/ml, respectively, were stirred at least 24 hours at 80°C before spin-coating. The PF2 solution was deposited at high temperature (103°C) onto ZnO-coated substrates heated at the same temperature, using the following three-step program: 600 rpm/200 $rpms^{-1}$/20s, 800rpm/800$rpms^{-1}$/60s, 2000rpm/2000$rpms^{-1}$/60s. On the other hand, the EH-IDTBR solution was spin-coated onto ZnO-coated substrates at room temperature at 2000 rpm for 60s. The films were left to dry overnight at a pressure around 10^{-7} mbar.

The absorbance measurements were carried out using a Perkin Elmer Lambda 19 UV/Vis/NIR spectrophotometer in two-beams mode. ZnO-coated ITO glass substrates were taken first as references to extract the active layer absorbance.

2.2. Fabrication and Characterization of OPV devices.

OPVs were fabricated using different active layers in the inverted structure. PF2 was used as electron-donor material and $PC_{71}BM$ and/or EH-IDTBR as electron-acceptor material. The best [donor:acceptor] mass ratio appeared to be [1:1.5] for all blends (see below). The solutions were prepared as follows: a polymer concentration of 4.5 mg/ml in *o*-DCB was chosen and the $PC_{71}BM$ and/or EH-IDTBR were added to the PF2 in different proportions from 0% to 100% of the total acceptor weight. Then, the solutions were stirred at least 24 hours at 80°C then they were spin-coated at high temperature onto hot ZnO-coated substrates (prepared as described previously).

The active layer film thickness ranged from 100 nm to 150 nm as measured by profilometry. Finally, the top electrode consisting of a Molybdenum oxide (MoO_3: 7 nm)/Ag (120 nm) bilayer was thermally evaporated through a shadow mask under vacuum (less than 5×10^{-6} mbar). The active layer and top contact deposition as well as the OPVs characterizations were done in a nitrogen atmosphere in the glove box.

The (J-V) curves were measured using a Keithley 2400 source meter and an ABET TECHNOLOGIES Sun 3000 solar simulator. The light intensity was calibrated to obtain 1 sun (AM 1.5 G, 100 mW/cm²) using a silicon calibration cell. The exposed device area (12 mm^2) was defined by a mask.

The device spectral response was measured inside the glove-box using a home-made setup using an Oriel 150 W solar simulator, a Jobin Yvon microHR monochromator (5 nm resolution) and a calibrated Si photodiode fitted after a beam-splitter to measure the incident light power for each wavelength band.

The OPV photostability was tested using a home-made whited LED lamp setup allowing an illumination of 100 mW/cm^2 in the (400-900 nm) wavelength range. The photovoltaic parameters were measured using our calibrated solar simulator after photo-degradation under the white LED in a controlled atmosphere (N_2 filled glove-box).

2.3. Charge Carrier Mobility Measurements.

Bottom contact bottom gate organic field effect transistor (OFET) structures were fabricated using commercially available silicon substrates. Lithographically defined Au (30 nm)/ITO (10 nm) bilayers were used as source and drain electrodes and 230 nm thick SiO_2 layer as a gate dielectric. Channel length and width were L = 20 µm and W = 10 mm, respectively. The substrates were cleaned sequentially under sonication with hellmanex, acetone, isopropanol at 45°C for 15 min each step followed by nitrogen drying and UV-ozone treatment for 15 min.

In the glove box, the surface of SiO_2 was treated with hexamethyldisilazane (HMDS, ALFA AESAR, 99+%) spin-coated then annealed at 135°C for 10 min. Finally, PF2:$PC_{71}BM$:EH-IDTBR blends were spin-coated at high temperature on hot substrates (≈100°C). A total concentration of 5mg/ml in *o*-DCB was used for each solution. Before characterization, OFET devices were dried overnight under a vacuum of 10^{-7} mbar. Afterwards, the output and transfer characteristics were carried out using a Keithley 4200 semiconductor characterization system. Hole mobilities were extracted in saturation regime using a standard device model.

The out-of-plane electron mobility was also extracted using space charge limited current (SCLC) devices. Electron-only devices were fabricated in the same way as solar cells, according to the following structures: Glass/ITO/ZnO/active layer/Ca(20nm)/Al(120nm). I-V curves were measured using a Keithley 4200 semiconductor characterization system. The mobilities were extracted by fitting the current density-voltage curves using the Mott-Gurney relationship.

2.4.Morphology and structural orientation measurements:

GIWAXS were performed at two synchrotron beamlines. GIWAXS measurements of pure materials films were conducted at PLS-II 9A U-SAXS beamline of Pohang Accelerator Laboratory (PAL) in Korea. The X-rays coming from the vacuum undulator (IVU) were monochromated using Si(111) double crystals and focused on the detector using K-B type mirrors. Patterns were recorded with a 2D CCD detector (Rayonix SX165). The sample-to-detector distance was about 225 mm for energy of 11.015 keV (wavelength: 1.1256 Å). The GIWAXS on binary blend films were conducted on the SIRIUS beamline at the French National Synchrotron Radiation facility SOLEIL in Saint-Aubin, France. An X-ray energy of 10 keV (wavelength: 1.24 Å) was selected with a Si(111) double crystal monochromator. 2D X-ray scattering data were collected on a DECTRIS PILATUS3 1M 2D detector positioned 472 mm downstream of the sample. In both cases, patterns were calibrated with standards, displayed and analyzed by using home-developed software.

Atomic Force Microscopy (AFM) measurements were carried out using the NanoObserver microscope from CSInstruments. The acquisition of the images was done on different locations of the sample and performed in tapping mode with a resolution of 512 x 512 px; images were processed with the Gwyddion free SPM data analysis software. The probes are supplied by AppNano and typically made of silicon.

3. Results and Discussion:

The frontier energy levels for the different materials in the active layer have been determined as follow: the $\mathrm{HOMO_{CV}}$ was measured by cyclic voltammetry but the $\mathrm{LUMO_{opt}}$ was calculated by adding to $\mathrm{HOMO_{CV}}$ the optical band-gap as determined by the absorption onset in solid-state (Fig. 1).

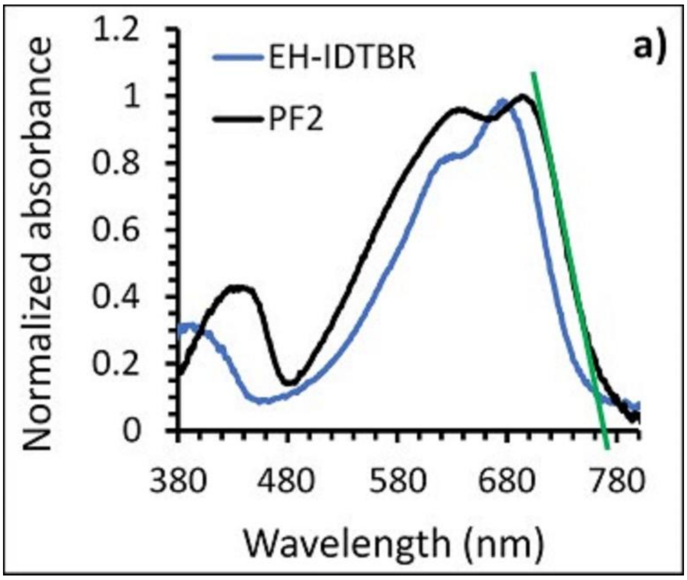

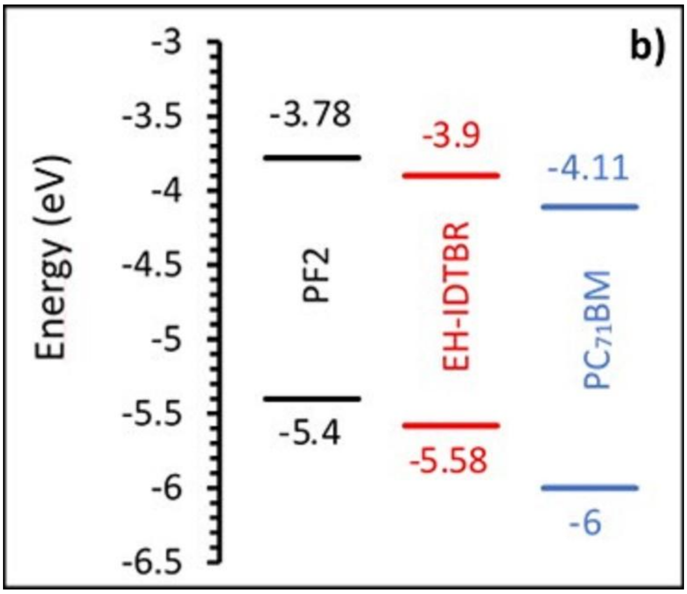

Fig. 1. (Single column) a) Normalized absorbance spectra in thin film for PF2 (black line) and EH-IDTBR (blue line). b) Frontier energy levels for the active-layer materials.

On the one hand, the frontier energy levels are adapted to use PF2 as electron-donor (D) and both EH-IDTBR and $PC_{71}BM$ as electron-acceptors (A) in an OSC. On the other hand, the absorption range is roughly the same for the electron donor (PF2) and the non-fullerene acceptor (EH-IDTBR) (Fig. 1a)). Both blends were tested as the active layer of an organic solar cell in an inverted structure in standard illumination conditions. After optimization, the best relative [D:A] mass ratio appeared to be [1:1.5] for all electron-acceptors. The main photovoltaic parameters are reported in Table 1 while the current-density (J) versus voltage (V) curves can be found in Fig. 2.

Blend	V_{oc} (V)	J_{sc} (mA/cm²)	FF (%)	PCE (%)
[PF2:$PC_{71}BM$]	0.75	15.0	74.4	8.4 (8.2)
[PF2:EH-IDTBR]	1.07	10.1	54.4	5.9 (5.6)

Table 1. Photovoltaic parameters of the [PF2:$PC_{71}BM$] and [PF2:EH-IDTBR] ([1:1.5]) OSC devices, measured on 12 mm² photodiode area in the inverted structure and under the standard illumination (AM 1.5 G, 100 mW/cm^2). The PCE value between parentheses is the average efficiency measured on at least eight different photodiodes.

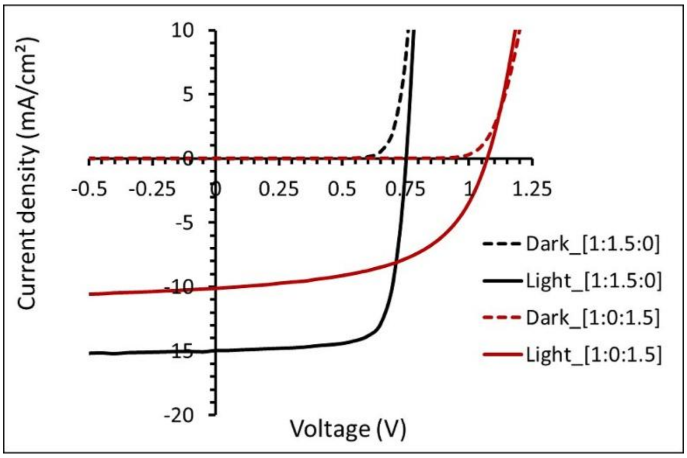

Fig. 2. (Single column) (J-V) characteristics of the [PF2:$PC_{71}BM$] and [PF2:EH-IDTBR] photovoltaic devices measured on 12 mm² photodiode area in the inverted structure and under the standard AM 1.5 G (100 mW/cm^2) illumination.

It should be first noted that the photovoltaic results obtained with [PF2:$PC_{71}BM$] are slightly lower than the one already published with this blend [32]. This can be due either to batch to batch variation often observed in polymer-based OSCs or to the device structure used in the present work. Indeed, we used ZnO instead of PEIE (polyethylenimine ethoxylated) in our inverted structure. This choice was made to avoid the sample-to-sample variation often observed when using PEIE. The open-circuit voltage is larger for the [PF2:EH-IDTBR] OSC reaching almost 1.1 V compared to 0.75 V for the [PF2:$PC_{71}BM$] blend. This was anticipated as V_{oc} increases linearly with the energy difference between the HOMO of the electron-donor and the LUMO of the electron-acceptor (Fig. 1b)) [44]. On the contrary, both the short-circuit current density (J_{sc}) and the fill factor (FF) are significantly smaller for the [PF2:EH-IDTBR] OSC despite device intensive optimization. As seen in Fig. 1, PF2 and EH-IDTBR are absorbing in the same wavelength-range but the blend was chosen according to interesting preliminary results regarding the device stability (a relative loss in PCE lower than 10% after 300 h continuous illumination for encapsulated devices [43]). Nevertheless, the almost one third relative decrease observed for J_{sc} and FF when using the NFA can not only be explained by non-complementary absorption spectra.

One explanation for the high PCE observed with PF2 blended with $PC_{71}BM$ naturally arises from the mainly face-on orientation of PF2 backbones leading to a good hole extraction in the direction perpendicular to the substrate [37]. The thin film morphologies of the [PF2:$PC_{71}BM$] and [PF2:EH-IDTBR] blends have been analyzed by GIWAXS. As seen in Fig. 3, both blends displayed equivalent structure and morphology of PF2 domains than neat polymer ones. In particular, a lamellar periodicity of 22-23 Å associated to an around 10 nm correlation length and a mixed face-on/edge-on morphology with a high proportion of face-on (orange and blue labels respectively) is observed for every blend. Patterns moreover contained the characteristic scattering signatures of the domains of the acceptor, consisting in a broad scattering maximum around 4.7 Å for $PC_{71}BM$ and a sharp reflection at ca. 17.4 Å for EH-ITDBR. Therefore, no major change in morphology is observed when EH-IDTBR is used as electron-acceptor instead of $PC_{71}BM$.

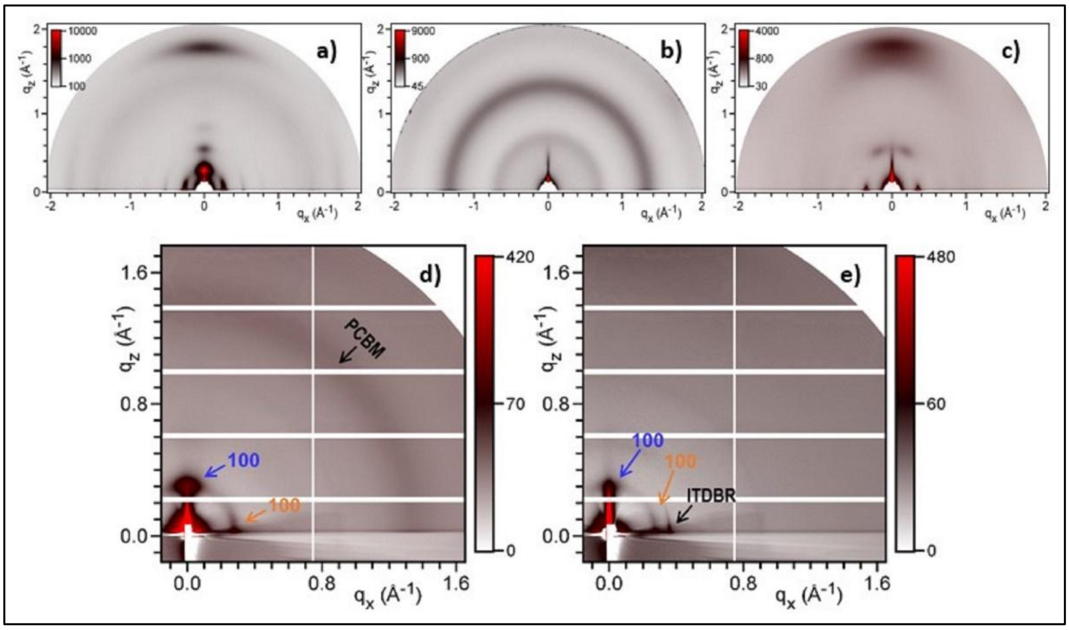

Fig. 3. (1.5 column) GIWAXS patterns for pure materials (top) and binary blends (bottom). Top line: a) PF2, b) $PC_{71}BM$ and c) EH-IDTBR. Bottom line: d) [PF2:$PC_{71}BM$] [1:1.5] and e) [PF2:EH-IDTBR] [1:1.5].

To further investigate the blend electronic properties, we measured the blend electron mobility both in the substrate plane (using organic field effect transistors or OFETs) and in the direction perpendicular to the substrate plane (using space charge limited current or SCLC diodes). The electron mobility calculated from the electrical characteristics on [1:1.5] [D:A] blends can be found in Table 2. While the in-plane electron mobility is rather high for every blend, the out-of-plane electron mobility is extremely low when using the NFA. This low electron mobility (around 6 x 10^{-6} cm^2/Vs) in [PF2:EH-IDTBR] blends in the direction of interest for the photovoltaic performances is in-line with the low J_{sc} and low FF measured when using the NFA. Such a low electron mobility perpendicular to the electrodes obviously points at a charge extraction limitation issue with these NFA-based OSCs.

Blend	**$\mu_{e\ OFET}$ (cm^2/Vs)**	**$\mu_{e\ SCLC}$ (cm^2/Vs)**
[PF2:$PC_{71}BM$]	(9.5 ± 2.0) x 10^{-4}	(3.0 ± 0.5) x 10^{-3}
[PF2:EH-IDTBR]	(6.0 ± 1.2) x 10^{-4}	(6.5 ± 1.5) x 10^{-6}

Table 2. Electron mobility in the substrate plane (OFET) and in the direction perpendicular to the substrate (SCLC) for [PF2:$PC_{71}BM$] and [PF2:EH-IDTBR] blends.

In order to test device stability, we used a white-light LED allowing a light intensity of 100 mW/cm^2. The OSC were continuously illuminated using this LED inside the glove-box in a N_2 atmosphere. Then (J-V) curves under standard illumination conditions (AM 1.5G 100 mW/cm^2) are measured to extract the photovoltaic parameters. Fig. 4 shows the light spectrum of both light-sources used for accelerated photo-degradation (LED) and the standard

AM1.5G photovoltaic characterization. As seen in Fig. 4, even if the integrated light power is the same (100 mW/cm^2), the LED source is much more intense in the active layer wavelength absorption range. We expected therefore to observe a photo-degradation in a reasonable time-scale using the LED source.

The normalized power conversion efficiency for both blends is plotted in Fig. 5 versus the LED continuous illumination time.

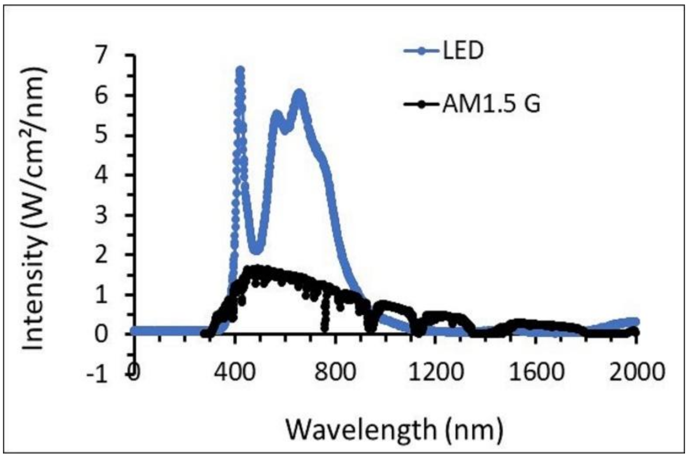

Fig. 4. (Single column) White LED light source spectrum (blue line) versus standard solar spectrum AM1.5 G (100 mW/cm^2) (black line).

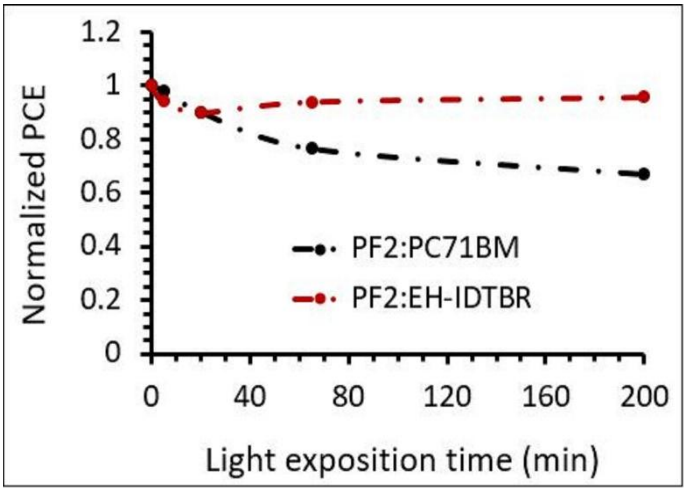

Fig. 5. (Single column) Normalized value of the power conversion efficiency under accelerated continuous illumination of the [PF2:PC$_{71}$BM] and [PF2:EH-IDTBR] OSC devices using the white light LED source.

Under continuous LED illumination, the OSCs behaved very differently. For the [PF2:PC$_{71}$BM] blend, a marked and continuous photo degradation is observed. 80% of the initial PCE is reached in only 40 minutes using accelerated photo-degradation on [PF2:PC$_{71}$BM] OSCs. On the contrary, after an initial small decrease in PCE during the first 40 minutes, the [PF2:EH-IDTBR] shows no measurable photo degradation, even after more than three hours of continuous LED illumination.

In an attempt to obtain higher efficiencies and a measurable increased stability, we further tried to use ternary blends, either with a very small proportion of PC$_{71}$BM or of NFA or with the same proportion of $PC_{71}BM$ and NFA but keeping in each case the [D:A] mass ratio constant. The variation of the photovoltaic parameters as a function of the added proportion of the EH-IDTBR to the binary blend [PF2:$PC_{71}BM$] is represented in Fig. 6 (Fig. S1 and Table S1 in the supporting information). Fig. 6a) shows a linear increasing tendency of V_{oc} with the increase of EH-IDTBR content and the V_{oc} values of the ternary blends are between those of the two binary blends. Devices exhibited a decreasing Jsc, FF, and PCE in the ternary blends followed then by their increase in [PF2:EH-IDTBR] blend (Fig. 6b,c,d)). Using an equivalent mass ratio of acceptor [1:0.75:0.75] for [PF2:$PC_{71}BM$:EH-IDTBR], the J_{sc} and the FF are higher than for the pure NFA-based [PF2:EH-IDTBR] device (11.7 mA/cm^2 and 57%, respectively). This observation is in-line with the twice higher out-of-plane electron mobility in the ternary blend about $(1.1 \pm 0.2) \times 10^{-5}$ cm^2/Vs (Table S2). Nevertheless, the V_{oc} is much lower in this ternary blend reaching only 0.86 V. Therefore, the high J_{sc} and FF in the ternary blend did not compensate the low V_{oc}. Consequently, the PCE is lower than using the NFA binary blend. The highest PCE using [PF2:$PC_{71}BM$:EH-IDTBR] blends was obtained with the [1:1.4:0.1] mass ratio (PCE of 6.8%). Then the V_{oc} is slightly higher than with [PF2:$PC_{71}BM$] (0.86 V compared to 0.75 V) but the J_{sc} and the FF decrease substantially (from 15.0 to 12.3 mA/cm^2 and from more than 74 to less than 71%) when using the low EH-IDTBR content ternary blend.

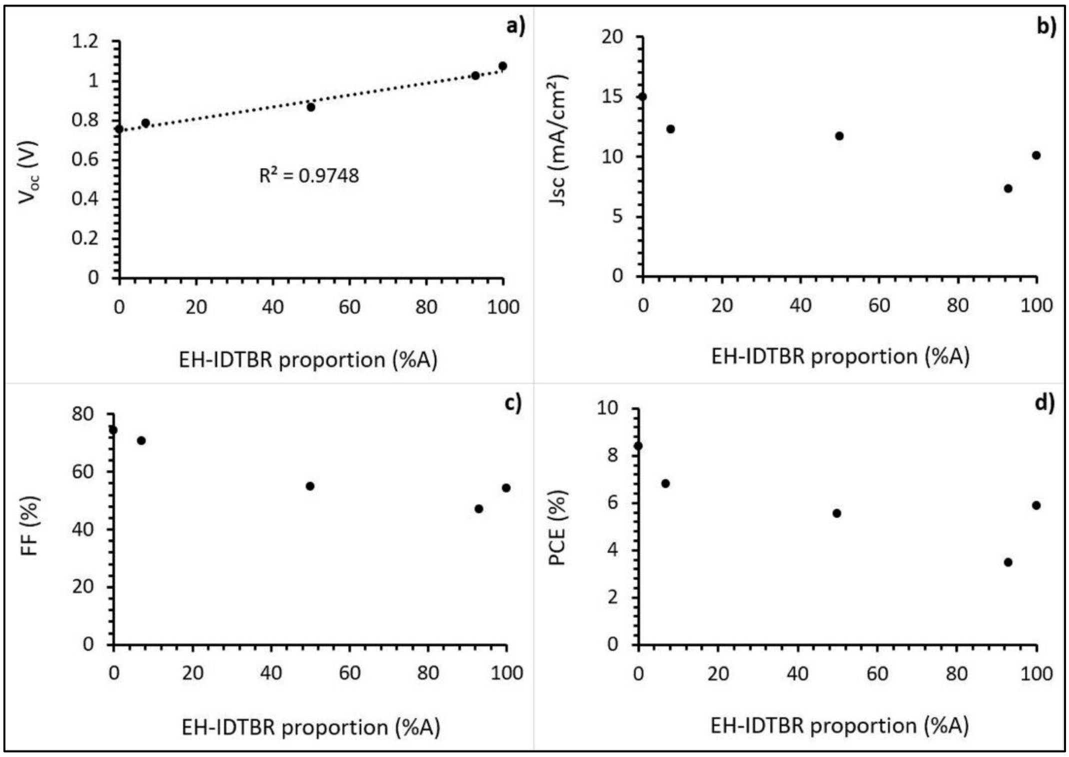

Fig. 6. (1.5 column) *Photovoltaic parameters variation as a function of the EH-IDTBR content (for the electron acceptor part) in [PF2:$PC_{71}BM$:EH-IDTBR] devices.*

The photovoltaic process in the ternary blend is governed by one of the four fundamental mechanisms, as shown in Fig. 7 [8,45,46]. The working mechanism is mainly related to the location of the third component against the host donor and acceptor and it could: (a) be fully embedded in the host donor or acceptor phase, (b) be at the interface between the host donor and acceptor phases, (c) forms a separated phase, and (d) forms an alloy phase with either the donor or acceptor. In the case (a), two possibilities are represented for low EH-IDTBR content, depending on if it is fully embedded in the donor (PF2) or acceptor ($PC_{71}BM$) phase. The high EH-IDTBR content will be schematically obtained by changing the red phase into the blue one and vice-versa. In case a), we assumed that PF2 and EH-IDTBR are the main light-absorbing materials and that an energy transfer that can occur between PF2 and EH-IDTBR.

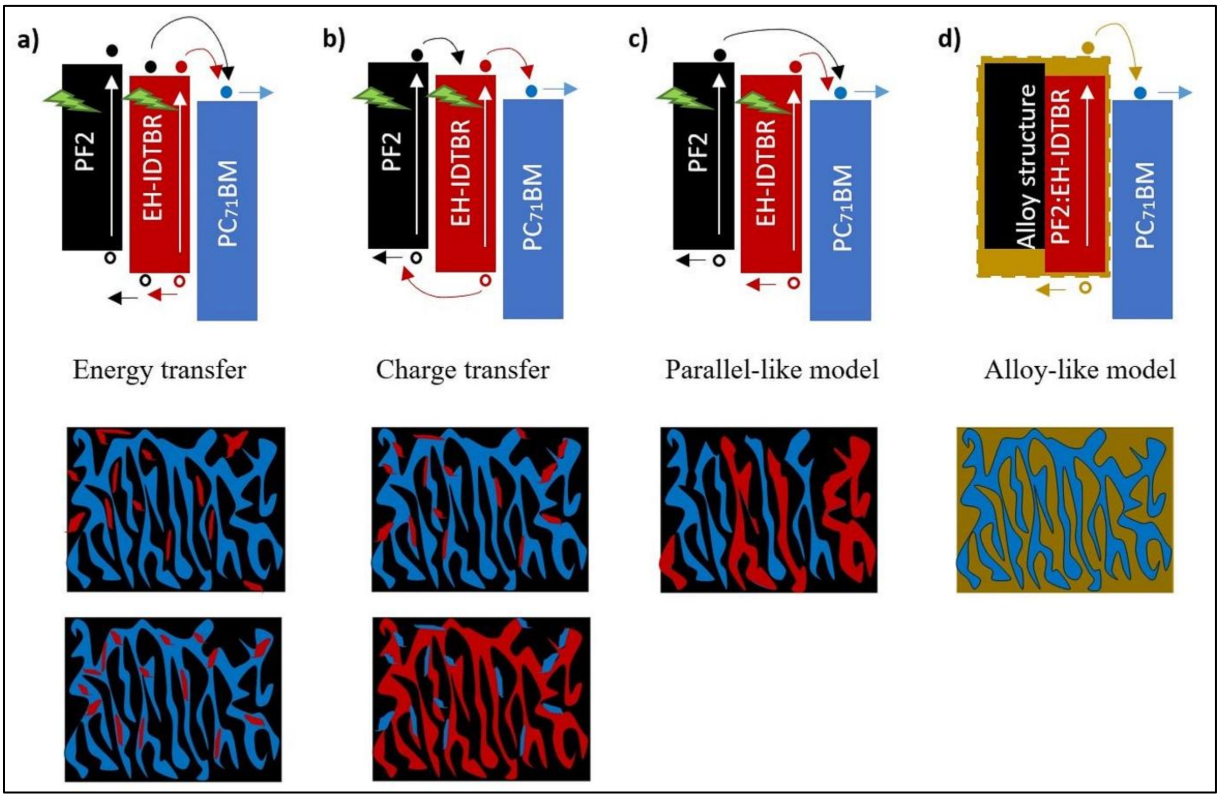

Fig. 7. (two column) Working mechanisms of the ternary BHJ blend (top) and the corresponding schematic morphology (bottom). a) represents the energy transfer mechanism, where it was assumed that PF2 and EH-IDTBR absorbed light to generate excitons. The energy can be transferred from PF2 to EH-IDTBR. The third component (EH-IDTBR) could be embedded in PF2 or $PC_{71}BM$. b) represents the charge transfer mechanism, where it was assumed that PF2 and EH-IDTBR absorbed light to generate excitons. The exciton-dissociation could take place at the PF2:EH-IDTBR or at the EH-IDTBR:$PC_{71}BM$ interface. The third component is located at the interface between the PF2 and $PC_{71}BM$ for low EH-IDTBR content ternary blends or at the interface between PF2 and EH-IDTBR for high EH-IDTBR content ternary blend. c) represents the parallel-like model where the miscibility between the three components is low. d) represents the alloy-like model where it was assumed that PF2 and EH-IDTBR formed an alloy.

The energy is transferred from the energy donor to the energy acceptor through the Dexter or Förster resonance energy transfer (FRET) mechanism [47], which requires the overlap between the emission of the energy donor and the absorption of the energy acceptor. This overlap is partially obtained in our case as shown in the supporting informations (Fig. S4). The energy transfer mechanism should be characterized by a continuous and almost linear increase of V_{oc} as a function of the EH-IDTBR content as observed here (Fig. 6a)). Further, J_{sc} should increase as a function of the EH-IDTBR content if this mechanism dominates but only if the light-absorption ranges of the two main absorbing materials are complementary

[48]. This is not the case in the present study (Fig. 1a)) and the observed decrease of J_{sc} (Fig. 6 b)) when the EH-IDTBR content increase is still compatible with the energy-transfer case.

The case b) is the charge transfer mechanism where the third component is located at the interface of the host matrix. Two extreme cases are represented for the schematic morphology depending if EH-IDTBR is the third low-content component in a PF2:$PC_{71}BM$ matrix or if $PC_{71}BM$ is the third low-content component in a PF2:EH-IDTBR matrix. In both cases, V_{oc} will be pinned to the lowest value measured in binary blends (here PF2:$PC_{71}BM$). Indeed, the electrons and holes are likely transferred to the material with the lowest LUMO and the highest HOMO, respectively, before the charge extraction. The V_{oc}, which is determined by the difference between these two energy levels [44], is expected to be pinned to the smallest value between those of the binary blends [49]. According to Fig. 6a), this is obviously not the case in the present study and the charge-transfer mechanism is probably not the dominant one.

When the tree components are not miscible and form their own domains in the ternary blend, the parallel-like mechanism (Fig. 7c)) could dominate. The ability of one material to dissolve another can be predicted based on their Hansen solubility parameters (HSPs) (dispersive solubility parameter (δ_D), the polar solubility parameter (δ_P), and the H-bonding solubility parameter (δ_H)) [46,50]. The relative energy difference (RED) between two materials allows determining their tendency to dissolve each other [51]. The related results as well as the relations used in the calculation are mentioned in Table S3. A RED < 1 was obtained for PF2 with both $PC_{71}BM$ and EH-IDTBR which indicates that PF2 has a high affinity for the two acceptors. In order to evaluate the miscibility between the tree materials, the Flory–Huggins interaction parameter (χ) was estimated from the Hansen solubility parameters [46,52] (see Table S4). The miscibility is expected to be good when $\chi < 0.3$ [53]. Here, good miscibility between the tree materials was obtained with χ of 0.11, 0.03, and 0.10 for PF2:$PC_{71}BM$, PF2:EH-IDTBR, and $PC_{71}BM$:EH-IDTBR, respectively. The parallel-like configuration (Fig. 7c)) is therefore not expected in our case.

Otherwise, an alloy-like morphology formation between two miscible acceptors (or donors) in $D:A_1:A_2$ (or $D_1:D_2:A$) ternary blend was reported, showing a linear evolving of V_{oc} with the third component proportion and an enhanced J_{sc} and FF [54–56]. In Fig. 7d), we assumed the alloy formation between PF2 and EH-IDTBR according to the lowest Flory-Huggins parameter for the PF2:EH-IDTBR blend. When the EH-IDTBR content is high, such alloy formation is in-line with the experimental data even though J_{sc} and FF are decreasing in our case (Fig. 6 b) and d)) when the proportion of EH-IDTBR increases.

In general, no mechanism really dominates in ternary blends and a mixture of the different mechanism takes place [46,57,58]. We can just rule out the charge-transfer mechanism and the parallel-like mechanism in our case. Further, according to solubility parameters, EH-IDTBR is most likely embedded in PF2.

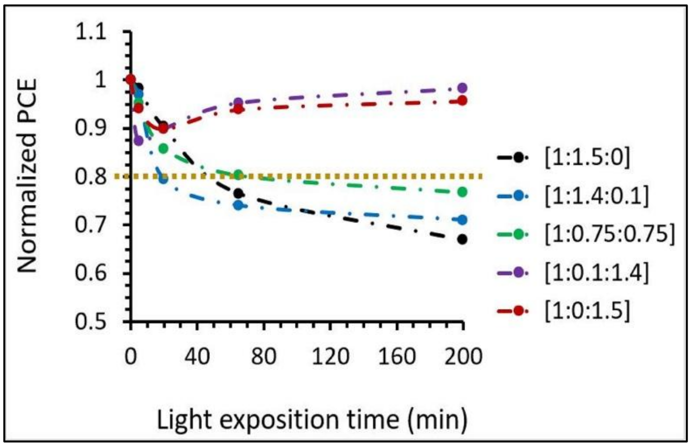

Fig. 8. (Single column) Normalized power conversion efficiency (PCE) versus the LED exposition time for the different [PF2:PC_{71}BM:EH-IDTBR] blends investigated and

The device stability is slightly improved for the low-EH-TDTBR content ternary blend as shown in Fig. 8) (blue discontinuous line) representing the evolution of the PCE as a function of the LED illumination time for the different blends. Therefore, the lower PCE in [1:0.1:1.4] [PF2:PC_{71}BM:EH-IDTBR] blend (Fig. 6d)) is not compensated by a substantially increased device stability (discontinuous line in purple) and a small proportion of EH-IDTBR is not the best compromise. From this study, it appears that the best blend to obtain a good stability with a reasonable efficiency is the [PF2:EH-ITBR] with a PCE in the 6% range and a limited photo degradation, even in harsh conditions.

To investigate the charge carriers' recombination processes, the dependence of J_{sc} and V_{oc} of [PF2:PC_{71}BM:EH-IDTBR] blends with the mass ratio of [1:1.4:0.1] and [1:0.1:1.4] at various incident light intensities (P_{in}) were studied before and after photo-degradation (Fig. 9). At the short circuit conditions, the J_{sc} follows the power-law dependence with the light intensity in the log-log scale represented by $J_{sc} \propto (P_{in})^{\alpha}$. Where the power (α) refers to the dominant recombination mechanism in the solar cells. The deviation of α from unity indicates that J_{SC} saturates rapidly with increasing light intensity [59]. In this case, the second-order bimolecular recombination is the dominant mechanism [60–63]. Whereas, if the dependence of J_{sc} on the light intensity (P_{in}) is linear with $\alpha \approx 1$, the bimolecular recombination is weak, leading to a quick charge carriers extraction in short-circuit conditions. Then, the recombination of charge carriers' is dominated by the first-order monomolecular recombination processes, including either Shockley-Read-Hall (SRH) recombination or geminate recombination [64]. Here, the fitting of the data yields $\alpha \approx 0.9$ in both [1:1.4:0.1] and [1:0.1:1.4] mass ratios of [PF2:PC_{71}BM:EH-IDTBR] blend, before photo-degradation (fig. 9a), indicating non-negligible bimolecular recombination losses, which is moreover not strongly affected by the photo-degradation process (Fig. 9c). Furthermore, in the open-circuit conditions, the light intensity dependence of V_{oc} in semi-log scale is represented with the following relation [65]:

$$V_{oc}\,(P_{in}) = n\,(KT/q)\,\mathrm{Ln}\,(P_{in}) + C$$

Where K is the Boltzmann constant, T is the temperature, q is the elementary charge, C is a constant, and n is the ideality factor. Indeed, n is an indication of the main recombination mechanisms present in a solar cell. The ideality factor (n) is close to 1 if the bimolecular recombination mechanism dominates, while 1< n <2 is observed when charge carriers' losses are dominated by the trap-assisted recombination mechanism [66]. Before photo-degradation, ideality factors (n) of 1.04 and 1.01 were obtained for [1:1.4:0.1] and [1:0.1:1.4] mass ratios of [PF2:$PC_{71}BM$:EH-IDTBR] blend, respectively. That refers to a dominating bimolecular recombination process in open-circuit conditions. However, n deviates from unity after photo-degradation, where [PF2:$PC_{71}BM$:EH-IDTBR] [1:1.4:0.1] blend shows a moderate increase of n reaching 1.13, which reveals the increases of trap-assisted recombination losses. The photo-degradation increases substantially the ideality factor in the high EH-IDTBR content ternary blend up to 1.42. Practically, for this blend, there is a change in the main charge-carrier recombination mechanism from bimolecular to trap-assisted in open-circuit conditions. Nevertheless, this high EH-IDTBR content ternary blend presents a much better photo-stability of the PCE. We could intuitively anticipate that the apparition of a large quantity of charge-carriers traps after photo-degradation could lead to a PCE degradation but it is obviously not the case in our system.

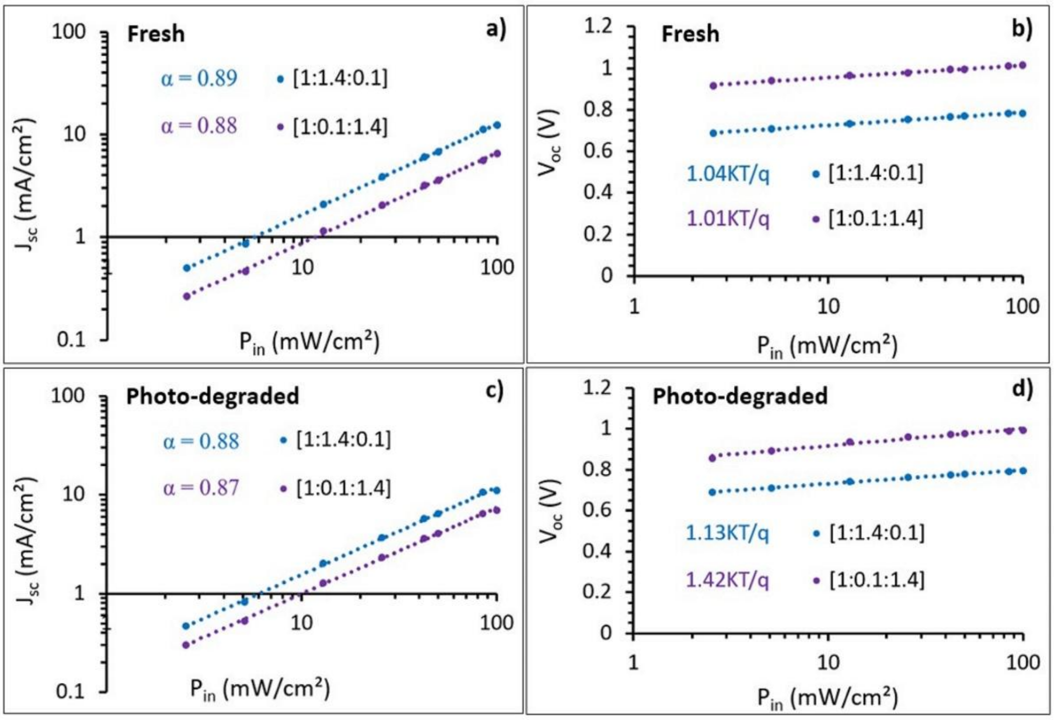

Fig. 9. (1.5 column) Light intensity (P_{in}) dependence of short-circuit current (J_{sc}) and open-circuit voltage (V_{oc}), respectively, a) and b) before photo-degradation, c) and d) after photo-degradation. Measurements were performed on 12 mm² photodiode area in the inverted structure.

In order to better understand the observed degradation, atomic force microscopy (AFM) was performed close to the top electrode of fresh and LED illuminated samples for three hours. Fig. 10 represents typical AFM topography images on ternary blends with a very small amount of one of the electron-acceptors. For fresh devices, the RMS is similar for both compositions and there is no marked difference in the domain sizes. After continuous LED illumination, PCBM rich devices shows a significant roughness increase with an apparent increase in domain size. EH-IDTBR-rich devices show the opposite behavior with a roughness reduction as well as a slight diminution in domain-size. This unexpected trend for EH-IDTBR-rich devices has been confirmed on several different samples and is reproducible. There seems to be a correlation between an observable morphology change toward larger domains and a higher roughness and the degradation of photovoltaic performances in PCBM rich samples while the roughness diminution and no appearance of large domains appears in similar time and temperature range in EH-IDTBR rich samples.

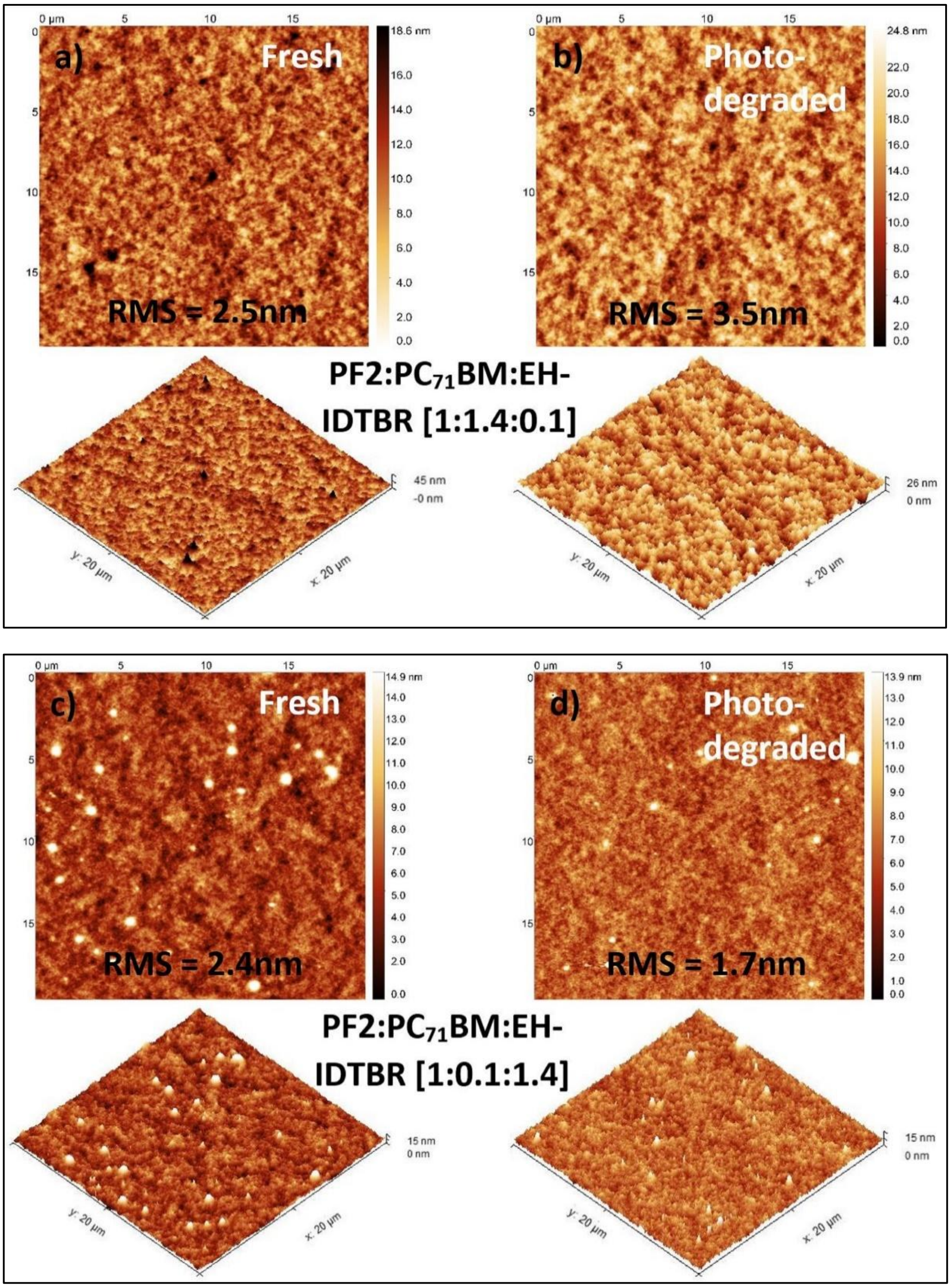

Fig. 10. (1.5 column) Atomic force microscopy (AFM) topography images (20 µm × 20 µm) before degradation a) and c) and after LED continuous illumination for three hours b) and d) for [PF2:PC_{71}BM:EH-IDTBR] devices with [1:1.4:0.1] and [1:0.1:1.4] mass ratio, respectively. RMS stands for Root Mean Square rugosity.

4. Conclusion:

Our study highlights the impact of electron acceptor on the efficiency and stability of their respective solar cells when blended with a fluorinated electron-donor polymer called PF2. Using the fullerene derivative ($PC_{71}BM$) as electron acceptor, the power conversion is high but the device stability in harsh-illumination conditions is significantly reduced. Using a NFA (EH-IDTBR), the power conversion efficiency is lowered but the device stability in the same conditions is highly improved. We have demonstrated, on the one hand, that using EH-IDTBR instead of $PC_{71}BM$ did not change the preferred face-on orientation of PF2 that was responsible for the high out-of-plane hole mobility and efficiency for [PF2:$PC_{71}BM$] blends. On the other hand, we measured a low out-of-plane electron mobility in [PF2:EH-IDTBR] blends in-line with the lower efficiency.

In order to achieve the best high efficiency/stability compromise, we tried to use ternary [PF2:$PC_{71}BM$:EH-IDTBR] blends. In our case, this approach did not lead to better results than the [PF2:EH-IDTBR] binary blends. Experimentally, we observed a lowering of the power conversion efficiency when adding EH-IDTBR in the blends. For high EH-IDTBR contents (more than 90% of the relative acceptor proportion), the stability is highly improved and accompanied by a change in the main charge-carrier recombination mechanism from bimolecular before photo-degradation to trap-assisted after photo-degradation. For the same samples, we observed after photo-degradation a diminution of the roughness without any extension of the domains size. For all other samples (with a relative EH-IDTBR content lower than 90% of the acceptor content) the main charge-carrier recombination mechanism is unchanged but the roughness and the domain-size is increased. It seems therefore that the main charge-carrier mechanism has a limited impact on the device stability. Thus, the stability appeared directly linked to the device nano-morphology.

Acknowledgements:

We thank Pohang Accelerator Laboratory (PAL) for giving us the opportunity to perform a part of the GIWAXS measurements, MEST and POSTECH for supporting these experiments, Dr Hyungju Ahn for adjustments and help, and other colleagues from the 9A USAXS beamline for assistance. We thank SOLEIL synchrotron for giving us the opportunity to perform the other GIWAXS measurements, Dr. Arnaud Hemmerle for adjustments and help, N. Aubert and other colleagues from SIRIUS beamline and SOLEIL for assistance.

The authors also thank the MATRIX SFR of the University of Angers and specifically the CARMA platform for the availability of the AFM.

Reference:

[1] Halls, J. J. M., Walsh, C. A., Greenham, N. C., Marseglia, E. A., Friend, R. H., Moratti, S. C., et al. Efficient photodiodes from interpenetrating polymer networks. Nature 376, 498–500 (1995). https://doi.org/10.1038/376498a0

[2] Song, J., Zhu, L., Li, C., Xu, J., Wu, H., Zhang, X., et al. High-efficiency organic solar cells with low voltage loss induced by solvent additive strategy. Matter 4, 2542–2552 (2021). https://doi.org/10.1016/j.matt.2021.06.010

[3] Liu, Y., Chen, C.-C., Hong, Z., Gao, J., (Michael) Yang, Y., Zhou, H., et al. Solution-processed small-molecule solar cells: breaking the 10% power conversion efficiency. Sci. Rep. 3, 3356 (2013). https://doi.org/10.1038/srep03356

[4] Liu, Y., Zhao, J., Li, Z., Mu, C., Ma, W., Hu, H., et al. Aggregation and morphology control enables multiple cases of high-efficiency polymer solar cells. Nat. Commun. 5, 5293 (2014). https://doi.org/10.1038/ncomms6293

[5] Zheng, Z., Zhang, S., Zhang, J., Qin, Y., Li, W., Yu, R., et al. Over 11% Efficiency in Tandem Polymer Solar Cells Featured by a Low-Band-Gap Polymer with Fine-Tuned Properties. Adv. Mater. 28, 5133–5138 (2016). https://doi.org/10.1002/adma.201600373

[6] Yuan, J., Zhang, Y., Zhou, L., Zhang, C., Lau, T., Zhang, G., et al. Fused Benzothiadiazole: A Building Block for n- Type Organic Acceptor to Achieve High- Performance Organic Solar Cells. Adv. Mater. 31, 1807577 (2019). https://doi.org/10.1002/adma.201807577

[7] Yuan, J., Zhang, Y., Zhou, L., Zhang, G., Yip, H.-L., Lau, T.-K., et al. Single-Junction Organic Solar Cell with over 15% Efficiency Using Fused-Ring Acceptor with Electron-Deficient Core. Joule 3, 1140–1151 (2019). https://doi.org/10.1016/j.joule.2019.01.004

[8] Lu, L., Kelly, M., You, W., Yu, L. Status and prospects for ternary organic photovoltaics. Nat. Photonics 9, 491–500 (2015). https://doi.org/10.1038/nphoton.2015.128

[9] Yu, R., Yao, H., Cui, Y., Hong, L., He, C., Hou, J. Improved Charge Transport and Reduced Nonradiative Energy Loss Enable Over 16% Efficiency in Ternary Polymer Solar Cells. Adv. Mater. 31, 1902302 (2019). https://doi.org/10.1002/adma.201902302

[10] Dai, S., Chandrabose, S., Xin, J., Li, T., Chen, K., Xue, P., et al. High-performance organic solar cells based on polymer donor/small molecule donor/nonfullerene acceptor ternary blends. J. Mater. Chem. A 7, 2268–2274 (2019). https://doi.org/10.1039/C8TA11637G

[11] Chen, S., Yan, T., Fanady, B., Song, W., Ge, J., Wei, Q., et al. High efficiency ternary organic solar cells enabled by compatible dual-donor strategy with planar conjugated structures. Sci. China Chem. 63, 917–923 (2020). https://doi.org/10.1007/s11426-020-9736-6

[12] Pan, M.-A., Lau, T.-K., Tang, Y., Wu, Y.-C., Liu, T., Li, K., et al. 16.7%-efficiency ternary blended organic photovoltaic cells with PCBM as the acceptor additive to increase the open-circuit voltage and phase purity. J. Mater. Chem. A 7, 20713–20722 (2019). https://doi.org/10.1039/C9TA06929A

[13] Zhang, C., Jiang, P., Zhou, X., Feng, S., Bi, Z., Xu, X., et al. Efficient Ternary Organic Solar Cells with a New Electron Acceptor Based on 3,4-(2,2-Dihexylpropylenedioxy)thiophene. ACS Appl. Mater. Interfaces 12, 40590–40598 (2020). https://doi.org/10.1021/acsami.0c11128

[14] Zhu, J., Cai, G., Xue, P., Jia, B., Zhang, C., Lu, X., et al. Effects of Side Chains in Third Components on the Performance of Fused-Ring Electron-Acceptor-Based Ternary Organic Solar Cells. Energy Fuels (2021). https://doi.org/10.1021/acs.energyfuels.1c02113

[15] Cheng, P., Zhan, X. Versatile third components for efficient and stable organic solar cells. Mater. Horiz. 2, 462–485 (2015). https://doi.org/10.1039/C5MH00090D

[16] Li, C., Zhou, J., Song, J., Xu, J., Zhang, H., Zhang, X., et al. Non-fullerene acceptors with branched side chains and improved molecular packing to exceed 18% efficiency in organic solar cells. Nat. Energy 6, 605–613 (2021). https://doi.org/10.1038/s41560-021-00820-x

[17] Cai, Y., Li, Y., Wang, R., Wu, H., Chen, Z., Zhang, J., et al. A Well-Mixed Phase Formed by Two Compatible Non-Fullerene Acceptors Enables Ternary Organic Solar Cells with Efficiency over 18.6%. Adv. Mater. n/a, 2101733 https://doi.org/10.1002/adma.202101733

[18] Cui, Y., Xu, Y., Yao, H., Bi, P., Hong, L., Zhang, J., et al. Single-Junction Organic Photovoltaic Cell with 19% Efficiency. Adv. Mater. n/a, 2102420 https://doi.org/10.1002/adma.202102420

[19] Salim, M. B., Nekovei, R., Jeyakumar, R. Organic tandem solar cells with 18.6% efficiency. Sol. Energy 198, 160–166 (2020). https://doi.org/10.1016/j.solener.2020.01.042

[20] Liu, G., Xia, R., Huang, Q., Zhang, K., Hu, Z., Jia, T., et al. Tandem Organic Solar Cells with 18.7% Efficiency Enabled by Suppressing the Charge Recombination in Front Sub-Cell. Adv. Funct. Mater. n/a, 2103283 https://doi.org/10.1002/adfm.202103283

[21] Aldersey-Williams, J., Rubert, T. Levelised cost of energy – A theoretical justification and critical assessment. Energy Policy 124, 169–179 (2019). https://doi.org/10.1016/j.enpol.2018.10.004

[22] Levelized Costs of New Generation Resources in the Annual Energy Outlook 2021. 25 (2021). https://www.eia.gov/outlooks/aeo/pdf/electricity_generation.pdf

[23] Jordan, D. C., Silverman, T. J., Wohlgemuth, J. H., Kurtz, S. R., VanSant, K. T. Photovoltaic failure and degradation modes. Prog. Photovolt. Res. Appl. 25, 318–326 (2017). https://doi.org/10.1002/pip.2866

[24] Compendium of photovoltaic degradation rates - Jordan - 2016 - Progress in Photovoltaics: Research and Applications - Wiley Online Library. https://onlinelibrary.wiley.com/doi/abs/10.1002/pip.2744

[25] Osterwald, C. R., McMahon, T. J. History of accelerated and qualification testing of terrestrial photovoltaic modules: A literature review. Prog. Photovolt. Res. Appl. 17, 11–33 (2009). https://doi.org/10.1002/pip.861

[26] Desombre, A. Methodology for a Reliability Study on Photovoltaic Modules. in Photovoltaic Solar Energy Conference (ed. Palz, W.) pp. 741–745 (Springer Netherlands, 1981). https://doi.org/10.1007/978-94-009-8423-3_117

[27] Mon, G. Predicting electrochemical breakdown in terrestrial photovoltaic modules. undefined (1984).

[28] Reese, M. O., Gevorgyan, S. A., Jørgensen, M., Bundgaard, E., Kurtz, S. R., Ginley, D. S., et al. Consensus stability testing protocols for organic photovoltaic materials and devices. Sol. Energy Mater. Sol. Cells 95, 1253–1267 (2011). https://doi.org/10.1016/j.solmat.2011.01.036

[29] Lee, J., Lee, J.-H., Yao, H., Cha, H., Hong, S., Lee, S., et al. Efficient and photostable ternary organic solar cells with a narrow band gap non-fullerene acceptor and fullerene additive. J. Mater. Chem. A 8, 6682–6691 (2020). https://doi.org/10.1039/C9TA14216A

[30] Xiao, J., Ren, M., Zhang, G., Wang, J., Zhang, D., Liu, L., et al. An Operando Study on the Photostability of Nonfullerene Organic Solar Cells. Sol. RRL 3, 1900077 (2019). https://doi.org/10.1002/solr.201900077

[31] Du, X., Heumueller, T., Gruber, W., Classen, A., Unruh, T., Li, N., et al. Efficient Polymer Solar Cells Based on Non-fullerene Acceptors with Potential Device Lifetime Approaching 10 Years. Joule 3, 215–226 (2019). https://doi.org/10.1016/j.joule.2018.09.001

[32] Li, Y., Huang, X., Ding, K., Sheriff, H. K. M., Ye, L., Liu, H., et al. Non-fullerene acceptor organic photovoltaics with intrinsic operational lifetimes over 30 years. Nat. Commun. 12, 5419 (2021). https://doi.org/10.1038/s41467-021-25718-w

[33] Kawano, K., Pacios, R., Poplavskyy, D., Nelson, J., Bradley, D. D. C., Durrant, J. R. Degradation of organic solar cells due to air exposure. Sol. Energy Mater. Sol. Cells 90, 3520–3530 (2006). https://doi.org/10.1016/j.solmat.2006.06.041

[34] Heumueller, T., Mateker, W. R., Distler, A., Fritze, U. F., Cheacharoen, R., Nguyen, W. H., et al. Morphological and electrical control of fullerene dimerization determines organic photovoltaic stability. Energy Environ. Sci. 9, 247–256 (2016). https://doi.org/10.1039/C5EE02912K

[35] Inasaridze, L. N., Shames, A. I., Martynov, I. V., Li, B., Mumyatov, A. V., Susarova, D. K., et al. Light-induced generation of free radicals by fullerene derivatives: an important degradation pathway in organic photovoltaics? J. Mater. Chem. A 5, 8044–8050 (2017). https://doi.org/10.1039/C7TA00175D

[36] Burlingame, Q., Huang, X., Liu, X., Jeong, C., Coburn, C., Forrest, S. R. Intrinsically stable organic solar cells under high-intensity illumination. Nature 573, 394–397 (2019). https://doi.org/10.1038/s41586-019-1544-1

[37] Ibraikulov, O. A., Ngov, C., Chávez, P., Bulut, I., Heinrich, B., Boyron, O., et al. Face-on orientation of fluorinated polymers conveyed by long alkyl chains: a prerequisite for high photovoltaic performances. J. Mater. Chem. A 6, 12038–12045 (2018). https://doi.org/10.1039/C8TA04127J

[38] Ibraikulov, Olzhas. A., Wang, J., Kamatham, N., Heinrich, B., Méry, S., Kohlstädt, M., et al. ITO- Free Organic Photovoltaic Modules Based on Fluorinated Polymers Deposited from Non- Halogenated Solution: A Major Step Toward Large- Scale Module Production. Sol. RRL 1900273 (2019). https://doi.org/10.1002/solr.201900273

[39] Holliday, S., Ashraf, R. S., Wadsworth, A., Baran, D., Yousaf, S. A., Nielsen, C. B., et al. High-efficiency and air-stable P3HT-based polymer solar cells with a new non-fullerene acceptor. Nat. Commun. 7, 11585 (2016). https://doi.org/10.1038/ncomms11585

[40] Cha, H., Wu, J., Wadsworth, A., Nagitta, J., Limbu, S., Pont, S., et al. An Efficient, “Burn in” Free Organic Solar Cell Employing a Nonfullerene Electron Acceptor. Adv. Mater. 29, 1701156 (2017). https://doi.org/10.1002/adma.201701156

[41] Lv, J., Feng, Y., Fu, J., Gao, J., Singh, R., Kumar, M., et al. Energetic Disorder and Activation Energy in Efficient Ternary Organic Solar Cells with Nonfullerene Acceptor Eh-IDTBR as the Third Component. Sol. RRL 4, 1900403 (2020). https://doi.org/10.1002/solr.201900403

[42] Wadsworth, A., Ashraf, R. S., Abdelsamie, M., Pont, S., Little, M., Moser, M., et al. Highly Efficient and Reproducible Nonfullerene Solar Cells from Hydrocarbon Solvents. ACS Energy Lett. 2, 1494–1500 (2017). https://doi.org/10.1021/acsenergylett.7b00390

[43] U. VONGSAYSY. ARMOR group. (Personal communication).

[44] Scharber, M. C., Mühlbacher, D., Koppe, M., Denk, P., Waldauf, C., Heeger, A. J., et al. Design Rules for Donors in Bulk-Heterojunction Solar Cells—Towards 10 % Energy-Conversion Efficiency. Adv. Mater. 18, 789–794 (2006). https://doi.org/10.1002/adma.200501717

[45] An, Q., Zhang, F., Zhang, J., Tang, W., Deng, Z., Hu, B. Versatile ternary organic solar cells: a critical review. Energy Environ. Sci. 9, 281–322 (2016). https://doi.org/10.1039/C5EE02641E

[46] Xu, X., Li, Y., Peng, Q. Recent advances in morphology optimizations towards highly efficient ternary organic solar cells. Nano Sel. 1, 30–58 (2020). https://doi.org/10.1002/nano.202000012

[47] Ito, J.-S., Goh, T., Li, X., Sfeir, M. Y., Bielinski, E. A., Tomasulo, S., et al. Polymer bulk heterojunction solar cells employing Förster resonance energy transfer. Nat. Photonics 7, 479–485 (2013). https://doi.org/10.1038/nphoton.2013.82

[48] Mohapatra, A. A., Tiwari, V., Patil, S. Energy transfer in ternary blend organic solar cells: recent insights and future directions. Energy Environ. Sci. 14, 302–319 (2021). https://doi.org/10.1039/D0EE03170D

[49] Ameri, T., Min, J., Li, N., Machui, F., Baran, D., Forster, M., et al. Performance Enhancement of the P3HT/PCBM Solar Cells through NIR Sensitization Using a Small-Bandgap Polymer. Adv. Energy Mater. 2, 1198–1202 (2012). https://doi.org/10.1002/aenm.201200219

[50] Hansen, C. M. *Hansen Solubility Parameters: A User's Handbook, Second Edition*. (CRC Press, 2007). https://doi.org/10.1201/9781420006834

[51] Walker, B., Tamayo, A., Duong, D. T., Dang, X.-D., Kim, C., Granstrom, J., et al. A Systematic Approach to Solvent Selection Based on Cohesive Energy Densities in a Molecular Bulk Heterojunction System. Adv. Energy Mater. 1, 221–229 (2011). https://doi.org/10.1002/aenm.201000054

[52] Leman, D., Kelly, M. A., Ness, S., Engmann, S., Herzing, A., Snyder, C., et al. In Situ Characterization of Polymer–Fullerene Bilayer Stability. Macromolecules 48, 383–392 (2015). https://doi.org/10.1021/ma5021227

[53] Langer, E., Bortel, K., Waskiewicz, S., Lenartowicz-Klik, M. 3 - Essential Quality Parameters of Plasticizers. in Plasticizers Derived from Post-Consumer PET (eds. Langer, E., Bortel, K., Waskiewicz, S., Lenartowicz-Klik, M.) pp. 45–100 (William Andrew Publishing, 2020). https://doi.org/10.1016/B978-0-323-46200-6.00003-9

[54] Khlyabich, P. P., Burkhart, B., Thompson, B. C. Efficient Ternary Blend Bulk Heterojunction Solar Cells with Tunable Open-Circuit Voltage. J. Am. Chem. Soc. 133, 14534–14537 (2011). https://doi.org/10.1021/ja205977z

[55] Khlyabich, P. P., Burkhart, B., Thompson, B. C. Compositional Dependence of the Open-Circuit Voltage in Ternary Blend Bulk Heterojunction Solar Cells Based on Two Donor Polymers. J. Am. Chem. Soc. 134, 9074–9077 (2012). https://doi.org/10.1021/ja302935n

[56] Kang, H., Kim, K.-H., Kang, T. E., Cho, C.-H., Park, S., Yoon, S. C., et al. Effect of Fullerene Tris-adducts on the Photovoltaic Performance of P3HT:Fullerene Ternary Blends. ACS Appl. Mater. Interfaces 5, 4401–4408 (2013). https://doi.org/10.1021/am400695e

[57] Lee, W., Kim, J.-H., Kim, T., Kim, S., Lee, C., Kim, J.-S., et al. Mechanically robust and high-performance ternary solar cells combining the merits of all-polymer and fullerene blends. J. Mater. Chem. A 6, 4494–4503 (2018). https://doi.org/10.1039/C7TA11382J

[58] Zhang, K.-N., Yang, X.-Y., Niu, M.-S., Wen, Z.-C., Chen, Z.-H., Feng, L., et al. Modulating the morphology and molecular arrangement via the well-compatible polymer donor in multiple working mechanisms interwined ternary organic solar cells. Org. Electron. 66, 13–23 (2019). https://doi.org/10.1016/j.orgel.2018.12.006

[59] Riedel, I., Parisi, J., Dyakonov, V., Lutsen, L., Vanderzande, D., Hummelen, J. C. Effect of Temperature and Illumination on the Electrical Characteristics of Polymer–Fullerene

Bulk-Heterojunction Solar Cells. Adv. Funct. Mater. 14, 38–44 (2004). https://doi.org/10.1002/adfm.200304399

[60] Zhenhua, S., Sitbon, G., Pons, T., Bakulin, A., Chen, Z. Reduced Carrier Recombination in PbS - CuInS2 Quantum Dot Solar Cells. Sci. Rep. 5, 10626 (2015). https://doi.org/10.1038/srep10626

[61] Lee, D., Lim, J., Park, M., Kim, J. Y., Song, J., Kwak, J., et al. The influence of sequential ligand exchange and elimination on the performance of P3HT:CdSe quantum dot hybrid solar cells. Nanotechnology 26, 465401 (2015). https://doi.org/10.1088/0957-4484/26/46/465401

[62] Jahandar, M., Khan, N., Jahankhan, M., Song, C. E., Hang Ken, L., Lee, S., et al. High-Performance CH3NH3PbI3 Inverted Planar Perovskite Solar Cells via Ammonium Halide Additives. J. Ind. Eng. Chem. 80, (2019). https://doi.org/10.1016/j.jiec.2019.08.004

[63] Lee, D., Kim, J., Park, G., Bae, H., An, M., Kim, J. Enhanced Operating Temperature Stability of Organic Solar Cells with Metal Oxide Hole Extraction Layer. Polymers 12, 992 (2020). https://doi.org/10.3390/polym12040992

[64] Bharti, V., Sharma, A., Gupta, V., Sharma, G. D., Chand, S. Improved hole mobility and suppressed trap density in polymer-polymer dual donor based highly efficient organic solar cells. Appl. Phys. Lett. 108, 073505 (2016). https://doi.org/10.1063/1.4942394

[65] Cowan, S. R., Roy, A., Heeger, A. J. Recombination in polymer-fullerene bulk heterojunction solar cells. Phys. Rev. B 82, 245207 (2010). https://doi.org/10.1103/PhysRevB.82.245207

[66] Mandoc, M. M., Kooistra, F. B., Hummelen, J. C., de Boer, B., Blom, P. W. M. Effect of traps on the performance of bulk heterojunction organic solar cells. Appl. Phys. Lett. 91, 263505 (2007). https://doi.org/10.1063/1.2821368